ChemComm

p - p orbital interaction via magnesium isovalent doping enhances optoelectronic properties of halide perovskites

Journal:	*ChemComm*
Manuscript ID	CC-COM-03-2020-002150.R2
Article Type:	Communication

COMMUNICATION

p - *p* orbital interaction *via* magnesium isovalent doping enhances optoelectronic properties of halide perovskites

Received 00th January 2019,
Accepted 00th January 2019

DOI: 10.1039/x0xx00000x

Feng Qian,[a,†] Jue Gong,[b,†] Mingyu Hu,[a,b] Chunyu Ge,[a] Nitin P. Padture,[b,*] Yuanyuan Zhou, [b,c,*] Jing Feng [a,*]

p - *p* orbital interaction through Mg (II) isovalent doping in methylammonium lead chloride perovskite significantly enhances the electronic properties while not affecting the optical bandgap. This chemical behaviour shows promising applications to optoelectronic devices.

Owing to the suitable optical bandgap of 2.9 eV, methylammonium lead trichloride ($CH_3NH_3PbCl_3$ or $MAPbCl_3$) perovskite is potentially useful in various applications such as deep-color light-emitting diodes, lasers, transparent photovoltaics, and ultraviolet (UV) photodetectors.[1-6] However, the high electronegativity of Cl^- can have adverse effect on the carrier mobilities of this perovskite material,[7] resulting in poor electronic properties and limiting the device performance. For mitigating this issue, composition engineering approaches may be used, which entail the replacement of either MA^+ or Cl^- with alternative ions.[8-13] But such practices inevitably bring about changes in the key optical bandgap of $MAPbCl_3$. For improving electronic properties, while maintaining the wide-bandgap nature, one can only resort to substitution of the B-site cations (Pb^{2+}) in $MAPbCl_3$. As a group 2A element, Mg^{2+} has a different valence electron configuration ($2s^22p^6$) from Pb^{2+} ($6s^2$). As shown in **Figure 1a**, when forming chemical bonds with Cl^- ($3s^23p^6$), the *p*-*p* orbital interaction between Mg^{2+} and Cl^- is expected to give rise to more polarizable electrons and thus higher carrier mobility because of greater spatial orbital overlap, as compared with the *s*-*p* interaction between Pb^{2+} and Cl^- shown in **Figure 1b**. Furthermore, due to relativistic effects, Pb 6*s* orbitals are phenomenally stabilized through spatial contraction,[14] which will additionally cause the bonding electrons in Pb-Cl network to be less mobile. In addition, in contrast to the $6s^2$ electrons of Pb^{2+}, the density distribution of $2p^6$ electrons of Mg^{2+} are in much closer proximity to the nucleus centre, contributing to tighter chemical bonding between Mg^{2+} and Cl^-, and thus, greater chemical stability of the perovskite.[15] As such, herein we demonstrate Mg-doping (**Figure 1c**) as a promising strategy for improving the electronic properties of $MAPbCl_3$ while maintaining its bandgap. Based on this approach, UV photodetectors with enhanced performance and stability are successfully demonstrated.

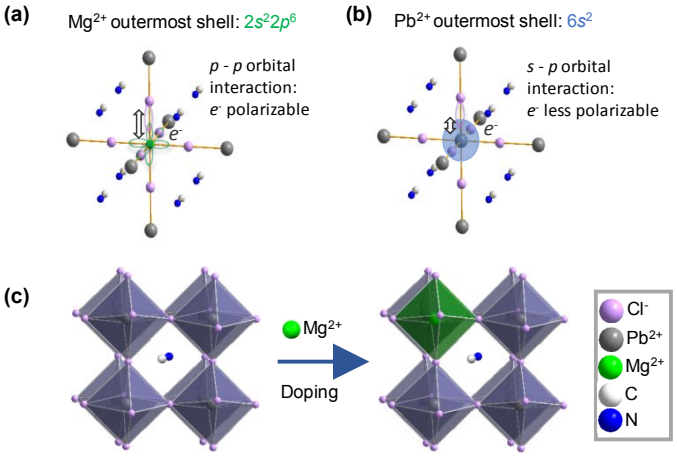

Figure 1. (b) Schematic illustrations of orbital interactions in (a) Mg-Cl bond and (b) Pb-Cl bond. (c) Schematic illustration of Mg-doping in $MAPbCl_3$ *via* cation substitution.

In order to confirm the Mg-doping mechanism in $MAPbCl_3$, we first synthesized Mg-doped $MAPbCl_3$ (denoted as Mg:$MAPbCl_3$) single-crystals using the antisolvent-vapor-assisted crystallization method.[16] Here, $PbCl_2$, MACl, and $MgCl_2$ are co-dissolved in dimethyl sulfoxide with molar ratios of 1:1:0.15 to form the precursor solution. Note here the atomic ratios in the precursor solution do not necessarily represent the composition of the final product. Subsequently, the solution was placed in an atmosphere of dichloromethane antisolvent vapor at room temperature, where the Mg:$MAPbCl_3$ single-crystals grow slowly. Pure $MAPbCl_3$ single-crystals were also grown without the addition of $MgCl_2$. More detailed experimental synthesis procedure is included in ESI. **Figure 2a**

[a] Faculty of Materials Science and Engineering, Kunming University of Science and Technology, Kunming, Yunnan 650093, China Email: jingfeng@kmust.edu.cn
[b] School of Engineering, Brown University, Providence, Rhode Island 02912, United States Email: nitin_padture@brown.edu
[c] Department of Physics, Hong Kong Baptist University (HKBU), Hong Kong SAR, China (Current Affiliation) Email: yyzhou@hkbu.edu.hk
† These authors contribute equally.
Electronic Supplementary Information (ESI) available. See DOI: 10.1039/x0xx00000x

compares the powder X-ray diffraction (XRD) patterns of ground samples of pure $MAPbCl_3$ and Mg:$MAPbCl_3$ single-crystals (inset shows photographs). Both samples show well-resolved XRD peaks that can be fully indexed based on the cubic $Pm\bar{3}m$ symmetry. Importantly, the characteristic (200) peak for Mg:$MAPbCl_3$ shifts to higher 2θ compared with that for pure $MAPbCl_3$, confirming a decrease of the lattice parameter (from a= 0.564 nm to a = 0.562 nm) of the cubic perovskite crystal structure. This suggests that ~2 at.% of Pb^{2+} (ionic radius: 119 pm) ions are substituted by Mg^{2+} (ionic radius: 72 pm) in the crystal structure according to Vegard's law.[17,18] We also studied the effect of Mg-doping amount on the phase and structure of Mg:$MAPbCl_3$ single-crystals. As shown in **Figure S1**, when the amount of Mg^{2+} precursors ($MgCl_2$) in the solution is increased, the lattice parameter is further reduced, indicating incorporation of more Mg^{2+} in the crystal structure. However, impurity phases are also identified in the resulting crystals with higher Mg-doping content, which can be attributed to phase segregation. In general, we do not observe a noticeable effect of Mg-doping on the macroscopic shape of as-grown $MAPbCl_3$, which is mostly related to the low doping level. The UV-vis absorption spectra of Mg:$MAPbCl_3$ and pure $MAPbCl_3$ are compared in **Figure 2b**, exhibiting the same band edge at ~430 nm. The corresponding Tauc plots in **Figure S2** reveal the same bandgap, 2.90 eV, in both Mg:$MAPbCl_3$ and pure $MAPbCl_3$ single-crystals. We further calculated density of states (DOS) for Mg:$MAPbCl_3$ and pure $MAPbCl_3$ as shown in **Figure 2c**, which again reveal the same bandgap for Mg:$MAPbCl_3$ and pure $MAPbCl_3$. This is because there are negligible effects of *s* or *p* orbitals of Mg on the Pb or Cl orbital energy levels near the bandgap (see **Figure S3** for more details).

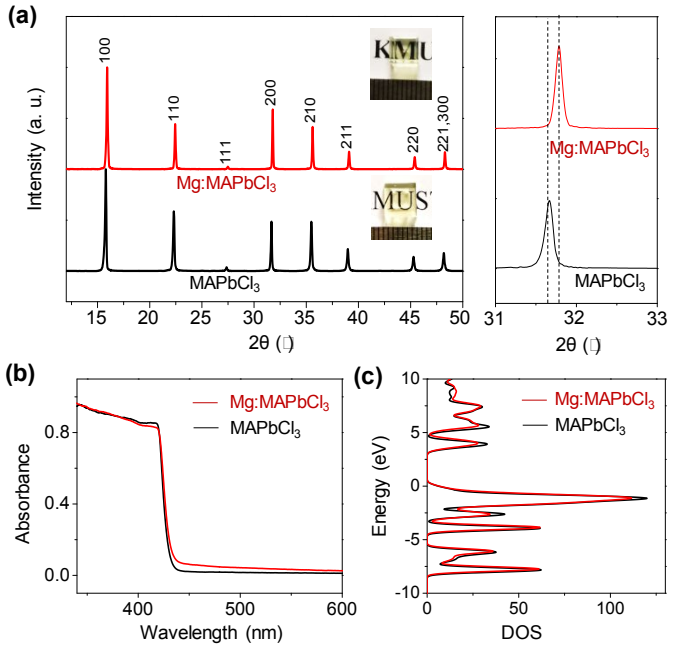

Figure 2. (a) XRD patterns of Mg:$MAPbCl_3$ and pure $MAPbCl_3$ samples prepared by grinding the single-crystals into fine crystallites. Insets are the photographs of the original single crystals. (b) UV-vis absorption spectra of Mg:$MAPbCl_3$ and pure $MAPbCl_3$ single-crystals. (c) DOS of Mg:$MAPbCl_3$ and pure $MAPbCl_3$ single-crystals.

X-ray photoelectron spectroscopy (XPS) studies were conducted to elucidate the effects of Mg-doping on the chemical bonding in the perovskite structure. As shown in **Figure 3a**, XPS survey scans confirm the existence of Pb, Cl, and C elements in both Mg:$MAPbCl_3$ and pure $MAPbCl_3$ single-crystal samples. By scrutinizing the binding energy region between 200 and 400 eV, we observed an intensity peak at ~300 eV that can be attributed to Mg KLL Auger photoelectrons [19] (**Figure 3b**), which attests the existence of Mg in Mg:$MAPbCl_3$. Furthermore, XPS resolution scans in **Figure 3c** reveal a larger binding energy of Cl 2*p* electrons in Mg:$MAPbCl_3$ than that in pure $MAPbCl_3$, which indicates that the conceptualized *p-p* orbital interaction brings forth a tight bonding in the Mg-Cl network. Meanwhile, we observed smaller binding energy of Pb 4*f* electrons in Mg:$MAPbCl_3$ (**Figure 3d**), which is consistent with moderated Pb-Cl connection by Mg-doping. Also, Cl 2*p* electrons show much smaller binding energy difference (0.04 eV) between Mg:$MAPbCl_3$ and $MAPbCl_3$ than Pb 4*f* electrons, which is attributed to the more polarizable *p-p* electrons in Mg-Cl bonds than the electrons in Pb-Cl bonds.

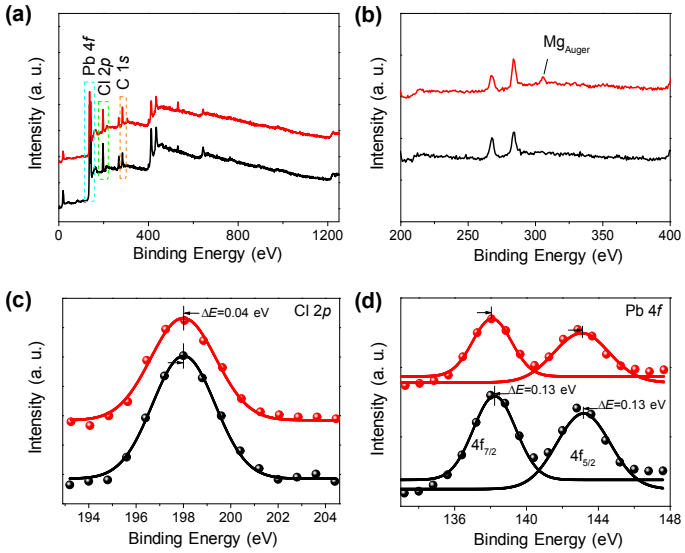

Figure 3. XPS spectra of Mg:$MAPbCl_3$ (red) and pure $MAPbCl_3$ (black) single-crystals: (a) survey scans and (b) zoomed-in view of survey scans. Higher resolution scans of: (c) Cl 2*p* and (d) Pb 4*f* electrons.

Lateral photoconductor-type electron-only devices (see **Figure S4** for the dimensions of interdigitated gold electrodes) based on Mg:$MAPbCl_3$ and pure $MAPbCl_3$ single-crystals were fabricated for understanding the effect of Mg-doping on the electronic properties. Under dark condition, space-charge-limited current (SCLC) measurements reveal a much lower trap-filled limit voltage (V_{TFL}) for Mg:$MAPbCl_3$ (0.337 V, **Figure 4b**) with respect to $MAPbCl_3$ single-crystal (1.460 V, **Figure 4a**). Correspondingly the trap density (n_{Trap}) of electrons in Mg:$MAPbCl_3$ is three times lower than that in pure $MAPbCl_3$ based on the following equation, [20]

$$n_{traps} = \frac{2\varepsilon_r\varepsilon_0 V_{TFL}}{qd^2}, \qquad (1)$$

where ε_r, ε_0, V_{TFL}, q, and d are the relative permittivity of $MAPbCl_3$ (23.9)[1,4], vacuum permittivity (8.854 x 10^{-12} F•m^{-1}), trap-filled limit voltage (V_{TFL}), elementary charge, and carrier drift length, respectively. Furthermore, electron mobility of Mg:$MAPbCl_3$ is determined to be 34% higher than that of pure $MAPbCl_3$ by fitting the child regimes in **Figure 4a** and **4b** using the following equation, [4]

$$J = \frac{9\varepsilon_r\varepsilon_0\mu V^2}{8d^3} \quad (2)$$

where μ, V, and J are carrier mobility, voltage, and current density, respectively. The photocurrent responses of photoconductor devices based on Mg:$MAPbCl_3$ and pure $MAPbCl_3$ single-crystals based are compared in **Figure 4c**. Upon the illumination of 365-nm UV photons with a power density of 0.0524 mW cm^{-2}, Mg:$MAPbCl_3$ single-crystal exhibits a photocurrent of 55 μA, which is much higher than $MAPbCl_3$ (38 μA). This unambiguously confirms the improved optoelectronic device performance due to Mg-doping.

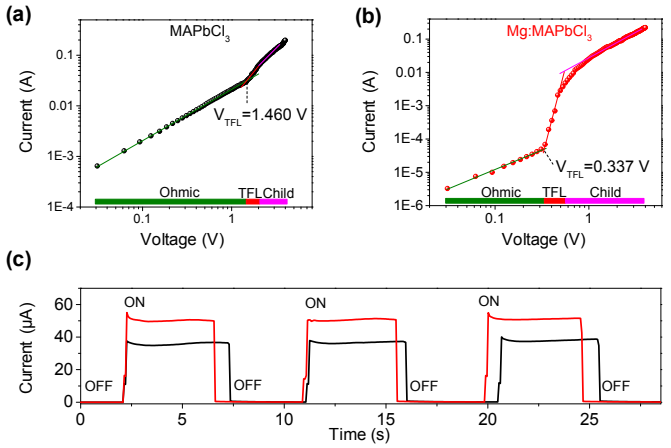

Figure 4. SCLC plots for single-crystals: (a) pure $MAPbCl_3$ and (b) Mg:$MAPbCl_3$. (c) On-off switching performance under 365-nm UV illumination of photodetectors based on pure $MAPbCl_3$ (black) and Mg:$MAPbCl_3$ (red) single-crystal.

Vertical thin-film photodetector-type devices are further fabricated by sandwiching the solution-processed halide perovskite layers with *n*-type and *p*-type charge extraction layers. The schematic illustrations showing the detailed device structures is included in **Figure S5**. Near-UV (450-nm) light illumination is used here. **Figures 5a** and **5b** show functional responses of photodetector devices based on Mg:$MAPbCl_3$ and pure $MAPbCl_3$ thin films, respectively, under varied incident power densities. **Figure 5c** plots the photocurrent density as a function of incident power density for the photodetectors based on **Figures 5a** and **5b**. It is clear that the Mg:$MAPbCl_3$-based photodetector outperforms the $MAPbCl_3$-based photodetector, particularly at higher power densities. **Figure 5d** compares the magnitude of photo-response of Mg:$MAPbCl_3$-based and pure $MAPbCl_3$-based photodetectors. Once again, the Mg:$MAPbCl_3$-based photodetector performs significantly better at high power densities (>0.13 W/cm^2).

Mg-doping also improves the stability of $MAPbCl_3$ perovskite, which is important for the operation of electronic devices. We monitored the evolution of absorption spectra for Mg:$MAPbCl_3$ and $MAPbCl_3$ thin films in a controlled environment (80% relative humidity; 30 °C; air). By tracking the maximum absorbance near 400 nm (**Figure S7**), it is evident that the Mg:$MAPbCl_3$ thin film retains more than 60% of the original absorbance after a period of storage in the ambient air, as compared to only 25% for pure $MAPbCl_3$. The storage time is 3 h, which is sufficient for this stability comparison. In terms of device stability (**Figure S8**), the Mg:$MAPbCl_3$ thin film photodetector has stabilized photocurrents above 90% of original magnitude during a 25-s continuous output under 450-nm illumination at incident power densities of 0.02 W.cm^{-2} and 0.09 W cm^{-2}. For comparison, less than 80% of the original currents are retained for the pure $MAPbCl_3$ device under the same test conditions. The observed material and device photocurrent stabilities corroborate the tighter atomic bonding as imparted by structural analyses mentioned earlier.

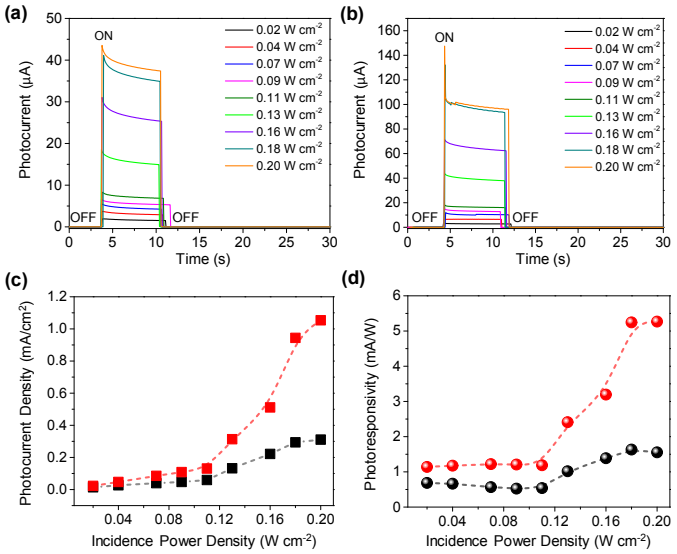

Figure 5. On-off switching performance under 450-nm light illumination with different incidence power densities of thin-film photodetectors based on: (a) pure $MAPbCl_3$ and (b) Mg:$MAPbCl_3$. Corresponding performance comparisons of the two types of thin-film photodetectors: (c) photocurrent density and (d) photoresponse.

In closing, we have demonstrated Mg-doping as an effective method for enhancing electronic properties of $MAPbCl_3$ perovskites without affecting the critical optical bandgaps, which shows promising applications to high-performance photodetectors. While it is currently challenging to gain more insights into the detailed crystal and defect structures using high-resolution characterizations such as transmission electron microscopy, synchrotron, and spectroscopies primarily due to the soft nature of as-synthesized perovskite materials, [21] we envision that future research effort in this direction may eventually overcome such characterization obstacles and unveil the exact character of metal doping in perovskites. Finally, this work points to a promising direction in influencing the atomic orbital interaction and chemical bonding through rational metal-doping for halide perovskites with tailored properties.

Conflicts of interest

There are no conflicts to declare.

Acknowledgements

The research performed at Kunming University of Science and Technology is supported by the from National Natural Science Foundation of China (grant No. 11504146 and No. 51762028), Rare Metal Material Genetic Engineering Project of Yunnan Province (grant no. 2018ZE019). The research performed at Brown University is supported by US National Science Foundation (OIA-1538893).

Notes and references

1 T. Matsushima, F. Bencheikh, T. Komino, M. R. Leyden, A. S. D. Sandanayaka, C. Qin and C. Adachi, *Nature*, 2019, **572**, 502-506.
2 G. Xing, N. Mathews, S. S. Lim, N. Yantara, X. Liu, D. Sabba, M. Gratzel, S. Mhaisalkar and T. C. Sum, *Nat. Mater.*, 2014, **13**, 476-480.
3 G. Maculan, A. D. Sheikh, A. L. Abdelhady, M. I. Saidaminov, M. A. Haque, B. Murali, E. Alarousu, O. F. Mohammed, T. Wu and O. M. Bakr, *J. Phys. Chem. Lett.*, 2015, **6**, 3781-3786.
4 W. Wang, H. Xu, J. Cai, J. Zhu, C. Ni, F. Hong, Z. Fang, F. Xu, S. Cui, R. Xu, L. Wang, F. Xu and J. Huang, *Opt. Express*, 2016, **24**, 8411-8419.
5 E. Zheng, B. Yuh, G. A. Tosado and Q. Yu, *J. Mater. Chem C*, 2017, **5**, 3796-3806.
6 D. Liu, C. Yang and R. R. Lunt, *Joule*, 2018, **2**, 1827-1837.
7 J. E. Huheey, E. A. Keiter and R. L. Keiter, *Inorganic Chemistry: Principles of Structure and Reactivity*, 4th edition. New York: HarperCollins College Publishers, 1993.
8 Y. Chen, M. He, J. Peng, Y. Sun and Z. Liang, *Adv. Sci.*, 2016, **3**, 1500392.
9 J. Gong, X. Li, P. Guo, I. Zhang, W. Huang, K. Lu, Y. Cheng, R. D. Schaller, T. J. Marks and T. Xu, *J. Mater. Chem. A*, 2019, **7**, 13043-13049.
10 L. Wang, G. D. Yuan, R. F. Duan, F. Huang, T. B. Wei, Z. Q. Liu, J. X. Wang and J. M. Li, *AIP Adv.*, 2016, **6**, 045115.
11 D. Amgar, T. Binyamin, V. Uvarov and L. Etgar, *Nanoscale*, 2018, **10**, 6060-6068.
12 S. Draguta, O. Sharia, S. J. Yoon, M. C. Brennan, Y. V. Morozov, J. S. Manser, P. V. Kamat, W. F. Schneider and M. Kuno, *Nat. Commun.*, 2017, **8**, 200.
13 W.A. Dunlap-Shohl, Y. Zhou, N.P. Padture, D.B. Mitzi, *Chem. Rev.* 2019, **119**, 3193-3295.
14 J. Autschbach, *J. Chem. Phys.*, 2012, **136**, 150902.
15 N. Phung, R. Félix, D. Meggiolaro, A. Al-Ashouri, G. S. e Silva, C. Hartmann, J. Hidalgo, H. Köbler, E. Mosconi, B. Lai, R. Gunder, M. Li, K.-L. Wang, Z.-K. Wang, K. Nie, E. Handick, R. G. Wilks, J. A. Marquez, B. Rech, T. Unold, J.-P. Correa-Baena, S. Albrecht, F. De Angelis, M. Bär and A. Abate, *J. Am. Chem. Soc.*, 2020, **142**, 2364-2374.
16 D. Shi, V. Adinolfi, R. Comin, M. Yuan, E. Alarousu, A. Buin, Y. Chen, S. Hoogland, A. Rothenberger, K. Katsiev, *Science* 2015, **347**, 519-522.
17 R. D. Shannon, *Acta Cryst.* 1976, **A32**, 751-767.
18 Y. Zhou, Z. Zhou, M. Chen, Y. Zong, J. Huang, S. Pang, N.P. Padture, *J. Mater. Chem. A*, 2016, **4**, 17623-17635
19 A. Talapatra, S. K. Bandyopadhyay, P. Sen, P. Barat, S. Mukherjee and M. Mukherjee, *Physica C*, 2005, **419**, 141-147.
20 R. H. Bube, *J. Appl. Phys.* 1962, **33**, 1733.
21 (a) Y. Zhou, H. Sternlicht, N.P. Padture. Joule 2019, 3, 641; (b) Y. Zhou, H. Zhou, J. Deng, W. Cho, Z. Cai. *Matter* 2020, 2, 360; (c) S. Cai, Y. Zhou. *Joule* 2020 in press.

